Journal of Applied Physics

RESEARCH ARTICLE | MAY 08 2026

Strain-driven amorphization in $Al_{1-x}Y_xN$ thin films and lattice-engineering stabilization illustrated by $In_{1-x}Y_xN$

Special Collection: Frontiers in Nitride Semiconductors Research

N. Afshar ; N. Wolff ; F. Hörich ; P. Straňák ; L. Kirste ; L. Kienle ; A. Dadgar ; O. Ambacher

Check for updates

J. Appl. Phys. 139, 185703 (2026)
https://doi.org/10.1063/5.0331741

View Online Export Citation

Articles You May Be Interested In

Experimental demonstration of wurtzite to rock salt transition and bandgap evolution in $In_{1-x}Sc_xN$ grown by sputtering

J. Appl. Phys. (January 2026)

Electronic mobility, doping, and defects in epitaxial $BaZrS_3$ chalcogenide perovskite thin films

J. Appl. Phys. (August 2025)

Point defect reduction in wide bandgap semiconductors by defect quasi Fermi level control

J. Appl. Phys. (November 2016)

12 August 2026 04:35:45

AIP Publishing

Journal of Applied Physics ARTICLE pubs.aip.org/aip/jap

Strain-driven amorphization in $Al_{1-x}Y_xN$ thin films and lattice-engineering stabilization illustrated by $In_{1-x}Y_xN$

Cite as: J. Appl. Phys. **139**, 185703 (2026); doi: 10.1063/5.0331741
Submitted: 27 February 2026 · Accepted: 18 April 2026 ·
Published Online: 8 May 2026

View Online Export Citation CrossMark

N. Afshar,[1,a)] N. Wolff,[2] F. Hörich,[3] P. Straňák,[4] L. Kirste,[4] L. Kienle,[2] A. Dadgar,[3] and O. Ambacher[1]

AFFILIATIONS

[1]Power Electronics, Institute for Sustainable Systems Engineering INATECH, University of Freiburg, Emmy-Noether-Str. 2, D-79110 Freiburg, Germany
[2]Department of Materials Science, Kiel University, Kaiserstr. 2, D-24143 Kiel, Germany
[3]Otto-von-Guericke-Universität Magdeburg, Institut für Physik, Magdeburg, Germany
[4]Fraunhofer Institute for Applied Solid State Physics (IAF), Tullastraße 72, D-79108 Freiburg, Germany

Note: This paper is part of the Special Topic on Frontiers in Nitride Semiconductors Research.
[a)]**Author to whom correspondence should be addressed:** niloofar.afshar@inatech.uni-freiburg.de

ABSTRACT

Aluminum yttrium nitride ($Al_{1-x}Y_xN$) is known to grow amorphous at relatively low Y concentrations ($x \sim 0.3$), but the exact structural origin of this transition has not been examined at the nanoscale. In this work, we deposited a series of $Al_{1-x}Y_xN$ thin films ($x \sim 0.08$, 0.21, and 0.5) on an AlN buffer layer (~200 nm) grown on silicon (111) substrates in an ultra-high-vacuum sputtering system and performed a detailed transmission electron microscopy (TEM) investigation complemented by x-ray diffraction and depth-resolved time-of-flight secondary ion mass spectrometry (ToF-SIMS). ToF-SIMS confirmed a uniform distribution of Al and Y throughout each layer, eliminating compositional segregation as a possible cause of crystalline quality degradation. TEM revealed the onset of partial amorphization at Y concentrations as low as $x = 0.21$, and a fully amorphous film at $x = 0.5$. By contrast, an analogous series of $In_{1-x}Y_xN$ films, deposited by magnetron sputtering, maintains its wurtzite-type structure up to $x = 0.5$, in agreement with density functional theory predictions and confirming that a larger, softer host lattice suppresses the strain-driven amorphization observed in $Al_{1-x}Y_xN$. These results demonstrate that internal strain arising from the Al–Y atomic-radius mismatch is likely the primary factor destabilizing the wurtzite lattice of $Al_{1-x}Y_xN$ and that strain and host-lattice engineering offers a viable route to stabilize highly mismatched nitride alloys.

© 2026 Author(s). All article content, except where otherwise noted, is licensed under a Creative Commons Attribution (CC BY) license (https://creativecommons.org/licenses/by/4.0/). https://doi.org/10.1063/5.0331741

I. INTRODUCTION

Aluminum yttrium nitride ($Al_{1-x}Y_xN$) belongs to the emerging class of nitride alloys that combine a rich set of properties. Compared with binary aluminum nitride (AlN), $Al_{1-x}Y_xN$ exhibits a markedly larger piezoelectric coefficient d_{33},[1,2] possesses intrinsic ferroelectricity,[3] and shows a strong promise for high-electron-mobility-transistor (HEMT) technologies.[4] Research interest in $Al_{1-x}Y_xN$ emerged following the discovery of the remarkable properties of its closely related alloy, aluminum scandium nitride ($Al_{1-x}Sc_xN$). $Al_{1-x}Sc_xN$ has been shown to possess an exceptionally high piezoelectric coefficient compared to AlN, approximately 400% higher, making it a highly promising material for RF applications.[5] In addition, it exhibits ferroelectric properties, rendering it suitable for a large range of devices, including non-volatile memory.[6] Despite its outstanding physical properties, one of the main drawbacks of Sc-based alloys is the high production cost of Sc, which limits their wide-spread industrial adoption. Consequently, identifying alternative materials with comparable properties but lower cost has become a timely and important research direction within the nitride community.

12 August 2026 04:35:45

© Author(s) 2026

$Al_{1-x}Y_xN$ emerges as a promising candidate with the potential to rival $Al_{1-x}Sc_xN$, while offering advantages such as lower production costs and easier large-scale implementation. Density functional theory (DFT) simulations predict that $Al_{1-x}Y_xN$ should exhibit properties similar to those of $Al_{1-x}Sc_xN$. Specifically, it is expected to retain its wurtzite crystal structure up to approximately $x \approx 0.75$, beyond which a phase transition to the cubic rock salt structure is anticipated.[7] $Al_{1-x}Y_xN$ has already been investigated experimentally. Measurements on Y-alloyed AlN show a sizable increase of d_{33},[1,2] while ferroelectric switching has been observed at low Y concentrations ($x = 0.07$).[3] In addition, device level demonstrations have highlighted its promise for power electronics.[4,8,9] Despite this attractive functional properties, the synthesis of high-quality $Al_{1-x}Y_xN$ remains demanding; numerous reports point to difficulties in attaining phase-pure, epitaxial material at elevated Y concentrations.[2,10] The material shows expected physical properties at low Y concentrations, approximately $x < 0.3$. However, despite the predicted phase transition occurring at $x \approx 0.75$,[7] the highest experimentally achieved Y content maintaining the high quality wurtzite-type structure is still far below the predicted phase transition.[2,11] In the intermediate composition range, studies have reported amorphization of the layers.[2,12] Overall, the body of research on $Al_{1-x}Y_xN$, particularly regarding its growth, remains limited.

The difficulties in growing $Al_{1-x}Y_xN$ compared to $Al_{1-x}Sc_xN$ are speculated to arise from several factors. First, $Al_{1-x}Sc_xN$ may be thermodynamically more stable than $Al_{1-x}Y_xN$. Figure 1 presents the calculated absolute values of the formation energies of $Al_{1-x}Y_xN$ and $Al_{1-x}Sc_xN$ as a function of transition metal concentration. As shown, $Al_{1-x}Y_xN$ exhibits higher formation energy than $Al_{1-x}Sc_xN$ at similar alloy concentrations, indicating lower thermodynamic stability. Another contributing factor may be the

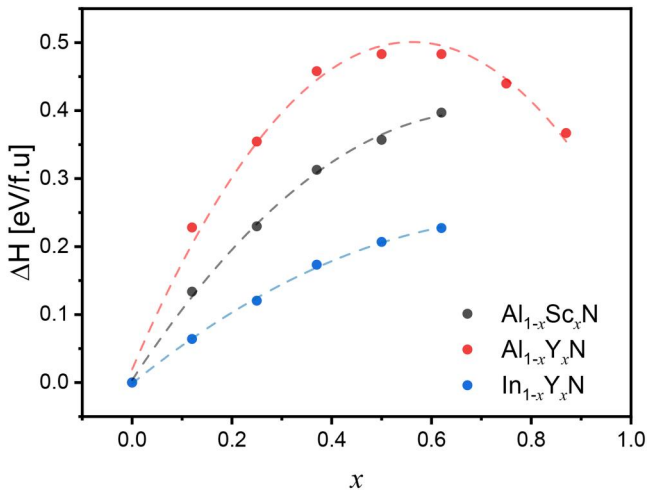

FIG. 1. Calculated formation energy of wurtzite $Al_{1-x}Y_xN$[7] (red), $Al_{1-x}Sc_xN$[16] (black), and $In_{1-x}Y_xN$[15] (blue) as a function of transition metal concentration. Dashed lines are polynomial fits to the data points given for a better guide for the eyes.

larger atomic radius mismatch between Y and Al compared to that between Sc and Al.[13] Incorporating the larger Y atoms into the wurtzite lattice of AlN introduces substantial lattice distortion, which can significantly reduce the stability of the wurtzite $Al_{1-x}Y_xN$ phase.[2,14] This lattice mismatch issue can be partially mitigated through strain-engineering approaches.[2] A complementary route is to select a host lattice in which the size mismatch between Y and group-III cation is intrinsically smaller. Indium nitride (InN) is an attractive candidate. Its lattice parameters (and bond lengths) are larger than those of AlN and its elastic stiffness is correspondingly lower,[15] so the incorporation of the larger Y atoms is expected to introduce less local distortion into the wurtzite framework. Consistent with this expectation, DFT calculations predict substantially lower formation energies for $In_{1-x}Y_xN$ across the same Y compositional range (Fig. 1), providing an additional thermodynamic rationale for the enhanced stability of $In_{1-x}Y_xN$.[15] To assess whether substituting AlN with InN improves the stability of the Y-containing alloy, we sputter-deposited a series of $In_{1-x}Y_xN$ films over a wide range of Y contents in this work.

In this context, it is also instructive to consider the concept of volume matching proposed by Tholander *et al.*,[17] which provides a more general framework for understanding alloy stability and functional properties in ternary nitrides. According to this approach, enhanced electromechanical response can be achieved when the constituent binary compounds have similar equilibrium volumes. In such cases, a flattening of the potential energy landscape occurs, facilitating structural transitions. Within this framework, the combination of Y and In is particularly favorable due to their comparable atomic volumes, whereas the large volume mismatch between Al and Y leads to significant internal strain in $Al_{1-x}Y_xN$. In addition to its superior structural and thermodynamic stability, $In_{1-x}Y_xN$ exhibits piezoelectric and elastic properties that are more favorable than those of $Al_{1-x}Y_xN$, making it a highly promising material for a variety of device concepts.[15,17] The combination of a large piezoelectric coefficient and a lower elastic stiffness further reduces the coercive field required to switch the polarization, positioning $In_{1-x}Y_xN$ as an attractive candidate for ferroelectric applications, where low voltage operation is essential.[15,17]

Another factor that can strongly influence the formation of crystalline $Al_{1-x}Y_xN$ is contamination, particularly with oxygen. Due to the high oxygen affinity of Y, oxygen can significantly impact the crystallization process.[10,18] To minimize the effect of oxygen on the growth and crystallinity of $Al_{1-x}Y_xN$, sputter deposition was performed in a high-vacuum chamber using ammonia (NH_3) as the reactive gas. Employing NH_3 instead of nitrogen (N_2) offers several advantages. When nitrogen used, N_2 molecules must first be dissociated into atomic nitrogen before bonding with the metal atoms. However, the nitrogen–nitrogen bond energy is relatively high (approximately 9 eV),[19] and at low pressures and temperatures, dissociation may be incomplete. This can lead to nitrogen deficiency, a high density of vacancies, and consequently heavily doped layers.[20,21] Nitrogen-deficient films are more susceptible to oxidation.[22,23] In contrast, the N–H bonds in NH_3 are weaker, allowing easier dissociation into reactive species, which can promote N-rich growth and the formation of stoichiometric nitrides. Additionally, the use of NH_3 introduces hydrogen (H_2)

12 August 2026 04:35:45

© Author(s) 2026

into the plasma. H_2 radicals can etch metallic or weakly bonded surface species during the film growth, altering ad-atom mobility and surface diffusion. Moreover, H_2 radicals can react with residual oxygen in the sputtering environment, potentially reducing oxygen incorporation in the deposited layers. Such effects have been widely reported in the growth of III-nitride materials, where NH_3-based processes often lead to enhanced crystallinity and surface quality compared to N_2-based growth under comparable conditions.

Following the growth of $Al_{1-x}Y_xN$ series in the UHV sputtering chamber, we complemented XRD measurements with detailed TEM analysis to track the evolution of crystalline structures as a function of Y content.

II. EXPERIMENTAL METHODS

The $Al_{1-x}Y_xN$ samples investigated in this study were grown by reactive pulsed-DC magnetron sputter deposition in an ultra-high-vacuum (UHV) system designed for the growth of metal-nitride compounds. The deposition chamber was equipped with two independent sputter sources, allowing co-sputtering from separate metallic Al and Y targets. 2-in. n-doped Si (111) wafers were used as the substrate. Si was selected as the substrate as its conductivity facilitates SEM/TEM investigations in the available setup. In order to screen the effect of the Si substrate on the $Al_{1-x}Y_xN$ layer, an AlN buffer layer was used. Prior to deposition, the silicon substrates were chemically cleaned to remove organic residues and the native oxide layer. The sputtering system has an upward-facing configuration, with the targets located at the bottom of the chamber and the substrates mounted face-down on a resistive heater. To ensure uniform film thickness and composition, a substrate rotation was applied throughout the deposition process.

Before film growth, the Al and Y targets were pre-sputtered in pure argon to remove surface contamination originating from previous depositions. High purity 2-in. metallic Al (6N purity) and Y (3N purity) targets were used. The base pressure of the chamber prior to deposition was approximately 5×10^{-8} mbar, minimizing unintentional incorporation of residual gases. The substrate was subsequently heated to 850 °C under a hydrogen atmosphere with a pressure of 1×10^{-2} mbar. The presence of hydrogen during the heating stage further assists in removing residual surface oxide from the silicon substrates and promotes a clean interface prior to film growth. Once the substrate temperature stabilized, an AlN layer was deposited. The thickness of the AlN layer was approximately 200 nm, chosen to ensure full relaxation and to provide a high-quality, oriented template for the subsequent growth of the ternary alloy. Further details on the buffer-layer growth are reported by Hörich *et al.*[24]

After the deposition of the AlN layer, the substrate temperature was reduced to 525 °C, and the growth of $Al_{1-x}Y_xN$ was initiated. This temperature was selected based on a preliminary series of growth experiments that identified 525 °C as the optimal condition for achieving the desired film quality. A series of samples with Y concentrations ranging from $x = 0$ to $x = 0.5$ was grown. The alloy composition was controlled by adjusting the relative sputtering power applied on the Al and Y targets, while keeping the total deposition time constant at one hour for all samples. The applied power on the Al target was kept unchanged at 100 W, and the applied power on the Y target was increased incrementally from 0 to 100 W. Reactive sputtering was carried out using purified ammonia (NH_3) as the nitrogen source, with getter-purified argon employed as the inert sputtering gas. A high Ar/NH_3 flow ratio of 20 (Ar: 100 SCCM and NH_3: 5 SCCM) was used in order to suppress target poisoning and maintain stable sputtering conditions. Following the growth of the $Al_{1-x}Y_xN$ layer and without changing the substrate temperature, an AlN capping layer was deposited without breaking the vacuum to protect the films from post-growth oxidation and moisture exposure. For samples with Y concentrations $x < 0.4$, a capping layer thickness of approximately 30–50 nm was used, whereas for the sample with $x = 0.5$, the cap thickness was increased to about 200 nm to ensure that post-growth oxidation is not affecting the high-Y samples. The total thickness of the $Al_{1-x}Y_xN$ layers ranged between 200 and 350 nm.

The $In_{1-x}Y_xN$ series was deposited in order to provide a direct comparison with the $Al_{1-x}Y_xN$ layers. Unlike the Al-based samples, which were grown in the dedicated nitride-UHV sputter system, the In-based samples were prepared in the same co-sputtering chamber (FHR) used for our earlier studies.[2,25] The machine is equipped with a pulsed-DC generator and accommodates separate 4-in. In (5N purity) and Y (5N purity) targets. Prior to deposition, each target was sputter-cleaned with pure argon to remove any residual contamination. This system is equipped with nitrogen (N_2) as the reactive gas and argon as the sputtering gas; the base pressure reached 4×10^{-7} mbar.

All films were grown on 2-in. *c*-plane sapphire substrates that first received a thin AlN buffer (approximately 20–30 nm) at 450 °C. Use of an AlN buffer layer allows for a straightforward comparison with the previously reported experimental data on $In_{1-x}Y_xN$ reported by Tholander *et al.*,[15] as they used the same staking strategy. Moreover, similar stacking was used for the other ternary nitrides such as $Al_{1-x}Sc_xN$, $Al_{1-x}Y_xN$, and $In_{1-x}Sc_xN$, studied in our previous works,[2,25] allowing to isolate the intrinsic stability of $In_{1-x}Y_xN$ and a direct compassion with other similar alloy systems. After the buffer layer deposition, the substrate was cooled to 250 °C and the deposition of $In_{1-x}Y_xN$ was started. The low temperature was chosen to prevent the back sublimation of $In_{1-x}Y_xN$ inside the sputtering chamber and to ensure the expected growth rate of the layers. The films were then capped using 50 nm AlN over-layer to prevent any post-growth oxidation. Since the deposition was done at relatively low temperatures, in order to ensure sufficient nitrogen dissociation, a high nitrogen to argon ration of 6 was used (N_2: 36 SCCM, Ar: 6 SCCM). The Y content was tuned by adjusting the sputtering power applied on In and Y targets. The Y target was operated between 0 and 500 W, while the In target was held between 20 and 60 W. The deposition was started from InN, as a well-studied reference sample, and the amount of Y was incrementally increased in the following samples.

Following deposition, the structural quality of samples was initially assessed using x-ray diffractometry (XRD). The lattice parameters of the $In_{1-x}Y_xN$ series were determined by measuring the diffraction peaks of the symmetric (0002) and asymmetric ($11\bar{2}4$) crystalline planes of the wurtzite phase. Measurements were

12 August 2026 04:35:45

© Author(s) 2026

carried out using an X'Pert MRT diffractometer (Panalytical) equipped with a CuK$_\alpha$ x-ray source. The ratio of Y to In atoms in $In_{1-x}Y_xN$ samples was determined using energy-dispersive x-ray spectroscopy (EDS).

Three representative $Al_{1-x}Y_xN$ samples with Y concentrations of $x = 0.08$, 0.21, and 0.5 were selected for detailed compositional analysis using time-of-flight secondary ion mass spectrometry (TOF-SIMS). Depth profiling were performed using an M6 Plus instrument (IONTOF GmbH, Germany) operated in a dual-beam mode. A 2 keV Cs^+ ion beam was used for sputtering, while a 30 keV Bi_1^+ primary ion beam was employed for analyzing the center of the crater. Ions were detected in a positive-ion mode as MCs^+ cluster ions, where M represents the element of interest. Both beams were incident at an angle of 45°. Film thicknesses were independently determined by cross-sectional scanning electron microscopy (SEM).

Transmission electron microscopy (TEM) was subsequently employed to investigate the structural evolution of the films on the nanometer scale using a probe aberration-corrected JEOL NEOARM microscope equipped with a dual-EDS detector system and a Continuum spectrometer. Cross-sectional lamellae were prepared by focused ion beam (FIB) milling. TEM analysis including electron diffraction, scanning TEM (STEM) using both annular bright-field (ABF) and high-angle annular dark-field (HAADF) signals and energy-dispersive x-ray spectroscopy (EDS) enabled a detailed examination of the crystalline quality, columnar growth morphology, and interfacial structure between the AlN layer and the $Al_{1-x}Y_xN$ layer as a function of Y concentration. In addition, electron energy-loss spectroscopy (EELS) measurements were carried out to probe the local chemical environment and to analyze the effect of Y incorporation in comparison to pure AlN. Spectra have been smoothed by a S-Golay filter.

III. STRUCTURAL AND COMPOSITIONAL ANALYSIS OF $Al_{1-x}Y_xN$

XRD θ–2θ scans performed on the $Al_{1-x}Y_xN$ samples are shown in Fig. 2. Figure 2(a) presents scans over a wide 2θ range for three Y concentrations, confirming the absence of secondary phases and indicating the presence of only wurtzite AlN and $Al_{1-x}Y_xN$. Figure 2(b) displays the 0002 reflections of the grown $Al_{1-x}Y_xN$/AlN heterostructures. Samples with $x = 0.08$ and 0.21 exhibit well-defined reflections that can be indexed to the wurtzite AlN and $Al_{1-x}Y_xN$ phase grown along the [0001] direction. In contrast, the film with $x = 0.5$ shows only the 0002 reflection associated with the underlying AlN layer; no additional reflections attributable to wurtzite or rock salt-type structures of $Al_{1-x}Y_xN$ are observed. This absence of Bragg reflections indicates that the $Al_{0.5}Y_{0.5}N$ layer is either fully amorphous or possesses a nanocrystalline structure with crystallites being too small to produce detectable diffraction. The emergence of an amorphous phase at high Y content has been reported previously, even when different optimization strategies were employed.[2] One approach that has shown limited success in stabilizing the wurtzite structure at higher Y concentrations is strain engineering.[2] The incorporation of large Y atoms into the relatively stiff AlN lattice likely generates

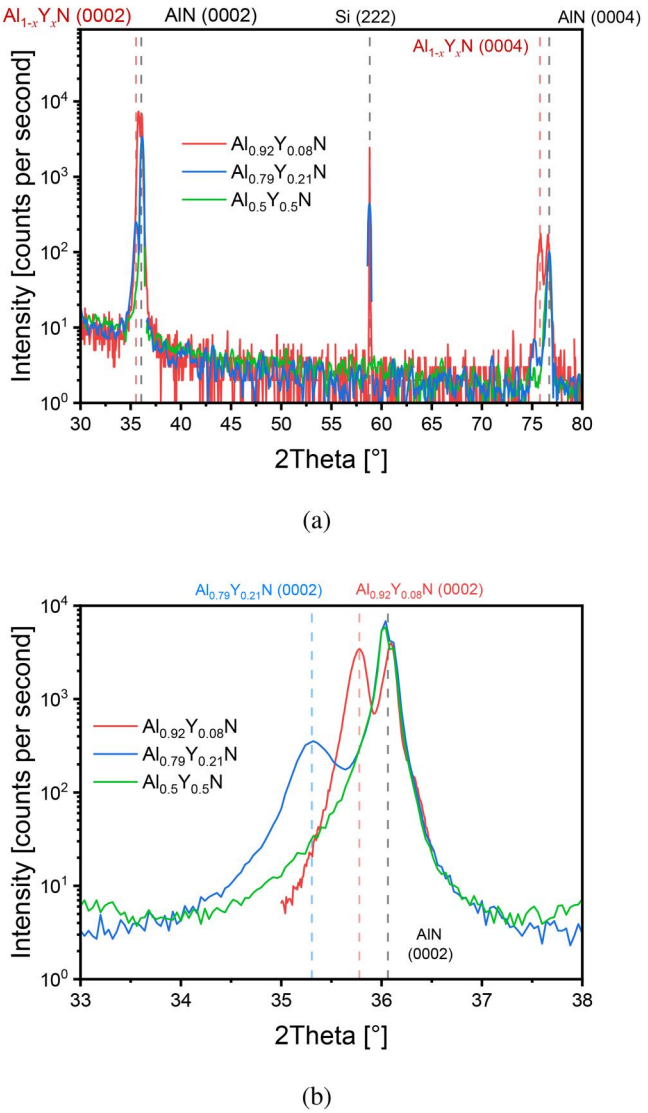

FIG. 2. Symmetric XRD measurements performed (a) on a wide 2θ range and (b) on the (0002) diffraction peak of wurtzite $Al_{1-x}Y_xN$ samples with different Y concentrations. In part (a), the presence of no secondary phases other than wurtzite AlN and $Al_{1-x}Y_xN$ can be seen. In part (b), the apparent doublet at the AlN (0002) peak corresponds to Cu Kα_1 and Kα_2, arising from the absence of a monochromator.

substantial lattice distortion, an effect that becomes more pronounced as the Y fraction increases.

To assess whether the observed amorphization is driven by compositional inhomogeneity (e.g., segregation of Y-rich regions or a concentration gradient) rather than intrinsic strain, depth-resolved ToF-SIMS was performed. Figure 3 displays the ToF-SIMS depth profiles of Y and Al for three $Al_{1-x}Y_xN$ samples, averaged from the measurements performed on three distinct

12 August 2026 04:35:45

© Author(s) 2026

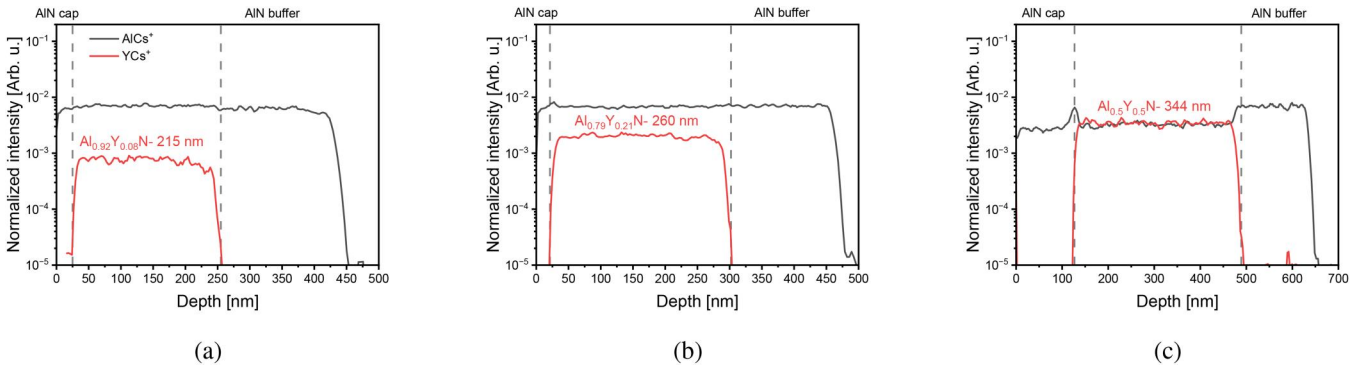

FIG. 3. ToF-SIMS depth profiles of $Al_{1-x}Y_xN$ samples with different Y concentrations (a) $x = 0.08$, (b) $x = 0.21$, and (c) $x = 0.5$. All signals were normalized to the Cs^+ ion signal, and a running average of three data points was applied. Different regions related to the AlN buffer layer, $Al_{1-x}Y_xN$ layer, and AlN capping layer are separated by dashed lines.

points of each sample. In all cases, the Y concentration remains essentially constant throughout the thickness of the $Al_{1-x}Y_xN$ layers, showing only a small gradient within the first few nanometers from the underlying AlN layer and the $Al_{0.92}Y_{0.08}N$ film. The Al signal likewise exhibits a flat distribution across the layer. The sharp transition between the AlN layer and the $Al_{1-x}Y_xN$ over-layer confirms the absence of interdiffusion or intermixing at the interface. It is assumed that a macroscopic compositional gradient or a phase separation would manifest as pronounced oscillations and steps in the ToF-SIMS trace. Thus, its absence allows us to rule out such large-scale segregation. These results demonstrate that the amorphous structure observed for the $Al_{0.5}Y_{0.5}N$ film cannot be ascribed to a concentration gradient or macroscopic phase separation; rather, it originates from an intrinsic instability of the highly Y-substituted lattice to retain long-range order under the imposed strain.

A cross-sectional ABF-STEM image and selected-area electron diffraction (SAED) pattern for the $Al_{0.92}Y_{0.08}N$ film are shown in Fig. 4. The thick AlN and the $Al_{0.92}Y_{0.08}N$ over-layer are clearly distinguished; both exhibit a columnar morphology. Mapping of the Y distribution by STEM-EDS shows a small compositional Y gradient along the film growth direction consistent to ToF-SIMS profiling. The SAED pattern recorded across both layers displays sharp diffraction spots that can be indexed to the hexagonal wurtzite-type symmetry of AlN and $Al_{0.92}Y_{0.08}N$, confirming epitaxial growth of $Al_{0.92}Y_{0.08}N$ on the AlN layer. The intensity of the out-of-plane and in-plane diffraction spots is split into two reflections correlated to the $Al_{0.92}Y_{0.08}N$ and AlN layers. For the alloyed film, overall larger lattice plane distances d of 0.6% and $\sim 2.1\%$ are determined, which agrees with the volumetric increase of the lattice by low-concentration Y incorporation.[2] HAADF-STEM images of the atomic structure at the $Al_{0.92}Y_{0.08}N$/AlN interface are shown in Fig. 5 and reveal metal(m)-polar growth continuation across a relatively abrupt and defect-free interface. The enhanced interface quality and epitaxial growth observed for the $Al_{0.92}Y_{0.08}N$/AlN heterostucture is attributed to the use of NH_3 as the reactive gas and the lower base pressure of the sputter chamber; such improvement was not seen in our earlier films deposited with N_2 as the reactive gas in a sputtering chamber with relatively higher base pressure.[2]

Quantitative analysis of the in-plane lattice spacing by geometric phase analysis indicates a strain gradient reaching across 10 nm from the interface which is accumulating to $\sim +2\%$ difference of the in-plane lattice parameter of $Al_{0.92}Y_{0.08}N$ relative to the AlN layer. This expansion is attributed to the elastic relaxation of the mismatched $Al_{0.92}Y_{0.08}N$ layer together with the slight compositional gradient and matches in extent to the lattice difference of the relaxed volume as measured by SAED.

Figure 6 presents the cross-sectional TEM image and the SAED pattern recorded on the $Al_{0.79}Y_{0.21}N$ film. The AlN layer retains its columnar texture, whereas diffraction contrast from crystalline regions in the $Al_{0.79}Y_{0.21}N$ layer are only observed close to the interface. The SAED pattern collected from the $Al_{0.79}Y_{0.21}N$ film shows broader wurtzite diffraction intensities and faint diffuse rings showing the poor crystalline texture at the interface and the latter characteristic of the amorphous fraction. Fast Fourier Transform patterns from HRTEM micrographs display (0001)-textured crystalline regions with poor structural coherence at the interface (~0–25 nm) of the $Al_{0.79}Y_{0.21}N$ layer. Beyond this thickness, the crystalline coherence further degrades, and by ~100 nm depth, the film becomes predominantly amorphous. The reduced intensity of the XRD 0002 reflection for this sample therefore originates solely from the remaining crystalline textured portion. In conclusion, at higher Y content ($x = 0.21$ compared to $x = 0.08$), relaxation is accompanied by a loss of crystallinity, underscoring the increased sensitivity of $Al_{1-x}Y_xN$ to strain-induced destabilization. This relaxation can be mitigated by employing a buffer layer that has a larger in-plane lattice parameter than AlN. Suitable options include other nitrides such as GaN or InN, or an $Al_{1-x}Y_xN$ buffer with a relatively lower Y content, as demonstrated previously.[2]

For the $Al_{0.5}Y_{0.5}N$ film, Fig. 7 shows the cross-sectional HAADF-STEM image together with Fast Fourier Transforms of

12 August 2026 04:35:45

© Author(s) 2026

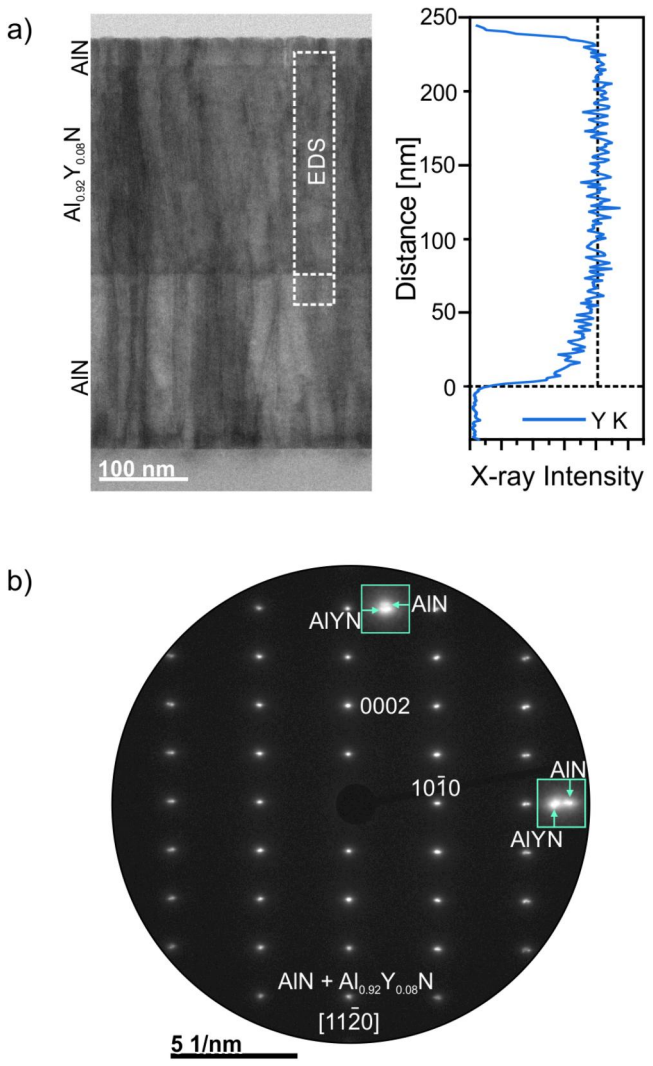

FIG. 4. (a) Cross-sectional ABF-STEM image and EDS Y-K profile. (b) SAED pattern recorded on the $Al_{0.92}Y_{0.08}N$/AlN layers. Both images confirm the columnar and coherent epitaxial crystalline structure of the $Al_{0.92}Y_{0.08}N$ layer.

the HRTEM image recorded from the $Al_{0.5}Y_{0.5}N$/AlN interface. The AlN layer maintains its columnar structure, whereas the $Al_{0.5}Y_{0.5}N$ over-layer lacks any discernible columnar morphology and exhibits a completely amorphous structure. The lack of crystalline areas corroborate the XRD observation that the film is amorphous rather than nanocrystalline. Analysis of the AlN capping layer (not shown) reveals that the cap grows polycrystalline on the underlying amorphous $Al_{0.5}Y_{0.5}N$ layer. STEM-EDS performed on the cross section reveals a comparative high oxygen concentration in the AlN capping layer, exceeding that measured in the $Al_{0.5}Y_{0.5}N$ layer itself. This elevated oxygen content is likely a consequence of the reduced protective efficiency of the polycrystalline cap, which permits diffusion of

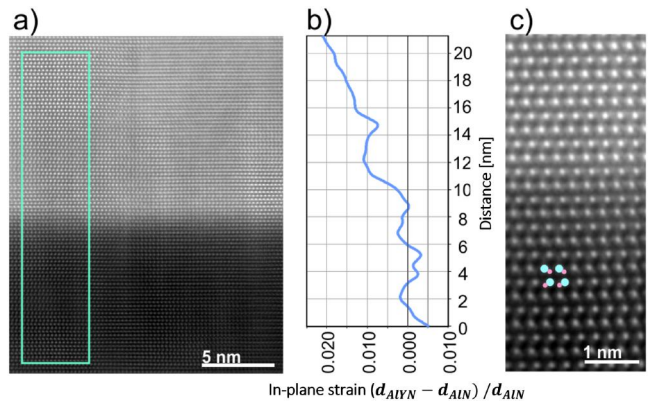

FIG. 5. Atomic-resolution imaging of the $Al_{0.92}Y_{0.08}N$/AlN interface. (a) HAADF-STEM showing epitaxial growth of the $Al_{0.92}Y_{0.08}N$ layer on the AlN layer. (b) Geometric phase analysis of the in-plane strain evolution across the interface showing an approximate of 2% increase in the in-plane lattice parameter. (c) HRSTEM-HAADF image of the atomic structure at the interface. The model sketch displays the metal-polar orientation of the AlN lattice.

ambient oxygen into the AlN, and subsequently the $Al_{0.5}Y_{0.5}N$ layer.

Further, a high density of void defects is observed at the $Al_{0.5}Y_{0.5}N$/AlN underlying layer interface together with a damaged region at the AlN surface [cf., Fig. 7(b)]. The $Al_{0.5}Y_{0.5}N$ sample required a higher power on the Y sputtering target, which can generate energetic Y atoms that impinge on the AlN layer surface and generate defect clusters during the initial stages of growth. Such defect nucleation may contribute to the premature loss of crystallinity in the high-Y film.

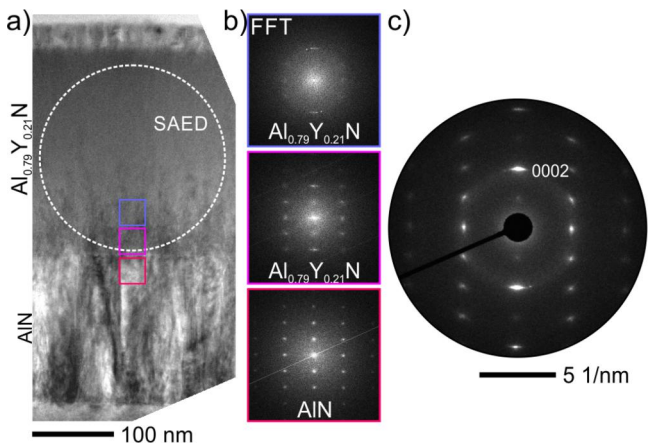

FIG. 6. (a) Cross-sectional TEM image of $Al_{0.79}Y_{0.21}N$/AlN layer, (b) FFT pattern from different regions across the interface, and (c) SAED pattern of the $Al_{0.79}Y_{0.21}N$ layer.

12 August 2026 04:35:45

© Author(s) 2026

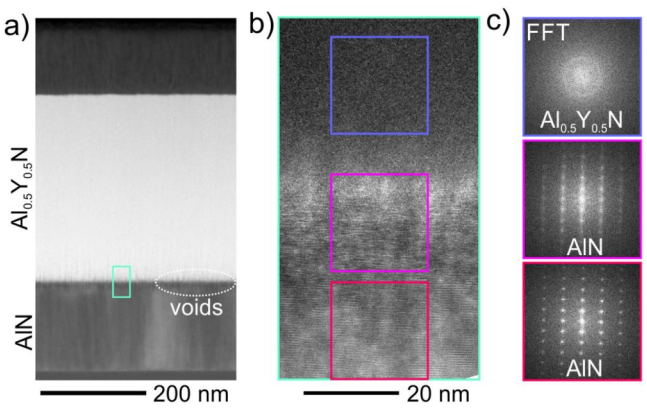

FIG. 7. (a) Cross-sectional HAADF-STEM image of the $Al_{0.5}Y_{0.5}N$/AlN sample. Void-defects are observed at the interface. (b) HRTEM image of the interface and (c) FFT patterns showing the distorted crystal structure of the AlN interface layer and the amorphous structure of the $Al_{0.5}Y_{0.5}N$ film.

Oxygen incorporation in the films was examined by the EDS and ToF-SIMS. The ToF-SIMS profiles (not included in the paper) revealed a uniform oxygen distribution throughout the thickness of each layer, indicating that the post-growth oxidation is negligible. Quantitatively, the oxygen signal from low-Y content films ($x = 0.08$ and 0.21) is essentially identical, whereas the high-Y sample ($x = 0.5$) exhibits oxygen concentration that is approximately three times higher. For the sample with $x = 0.5$, the AlN capping layer contains a noticeably higher oxygen content than the underlying $Al_{0.5}Y_{0.5}N$, which as discussed before, is attributed to the polycrystalline nature of the cap and its reduced protective capability. However, the absolute oxygen concentrations cannot be extracted with high numerical accuracy, as there is no suitable standard for measuring the oxygen content. Nevertheless, the fact that the $x = 0.08$ and $x = 0.21$ samples exhibit comparable oxygen contents while showing markedly different structural properties indicates that oxygen is not the dominant factor governing the degradation of crystallinity in this compositional range. Instead, this behavior points toward intrinsic strain- and lattice-distortion-related effects associated with increasing Y incorporation. It should be noted, however, that for the $x = 0.5$ samples, where a higher oxygen content is observed, a combined influence of intrinsic instability and oxygen incorporation on the amorphous structure cannot be excluded.

The concordant evidence from ToF-SIMS (uniform Y distribution), XRD (absence of reflections from crystalline volumes for $Al_{0.5}Y_{0.5}N$), and TEM (amorphous structure) demonstrates that, beyond a critical Y concentration, $Al_{1-x}Y_xN$ cannot sustain the wurtzite lattice and instead forms an amorphous solid solution. The transition is not driven by compositional gradients or phase separation, but is intrinsically linked to strain accommodation. Y substitution introduces local lattice distortion and residual stress within the wurtzite AlN framework due to the large size mismatch between Al and Y. Notably, first-principle calculations indicate that the wurtzite $Al_{1-x}Y_xN$ in this composition range satisfies the Born mechanical stability criteria,[26] implying elastic stability of the ideal crystalline structure. Nevertheless, our experiments consistently show a transition to fully amorphous growth at elevated Y concentrations, even under markedly different sputtering conditions.[2] This indicates that the observed amorphization is not an intrinsic instability of the ideal wurtzite lattice, but is driven by the cumulative build up of local strain and structural frustration associated with Y incorporation.

IV. EELS ANALYSIS ON $Al_{1-x}Y_xN$ SAMPLES

To probe how Y incorporation perturbs the local bonding and electronic structure of the nitrogen ions, we acquired electron-energy loss spectra of the N-K edge from crystalline regions of the three compositions ($x = 0$, 0.08, and 0.21). The spectra were collected at low electron dose to minimize radiation damage effects in the presence of oxygen doping.[27] The energy-loss near edge structure (ELNES) of the N-K edge is characteristic for the tetrahedral sp^3 environment within the wurtzite-type lattice and its fine structure shows variations from binary to ternary compounds.[28,29] The multi-peak structure of the ELNES reflects the unoccupied N 2*p*-derived states in the conduction band of nitrogen atoms and the *s*-, *p*- and *d*-orbital states of neighboring cations, which have significant *p* components projected onto the N sites.[28] The individual recorded N-K ELNES are shown in Fig. 8. The AlN reference recorded on the seed layer exhibits the expected sharp onset of the edge and a well-resolved multi-peak structure (with features *A*–*C*) based on the contribution of the out-of-plane p_z bond and the in-plane $p_{x,y}$ bonds.[30,31] The *A* feature is centered at ∼400 eV and the *C* peak at ∼405.5 eV. According to density-functional theory based on core-hole calculations, the intensity of the features *A* and the peak *B* is dominated by the number of unoccupied $p_{x,y}$ states and the core-hole charge bound at the N-site.[30] Further, contributions to feature *C* are mostly dominated by the p_z contribution.

Upon substitution of 8% ($x = 0.08$) and 21% ($x = 0.21$) Y, the overall shape of the N-K edge is mostly preserved, but becomes noticeably broader and subsequently reduces in total intensity compared to the first broad maximum seen in the high energy tail. The intensity of peak *A* is fairly reduced for higher alloying levels while the positions of peak *B* and peak *C* shift to lower energy. For instance, peak *C* shifts by ∼−0.5 eV upon alloying, which is possibly related to the small tensile strain along the *c* axis upon alloying.[32] These changes indicate a perturbation of the local symmetry and hybridization of N2*p* states with the directional orbitals of the metal sub-lattice and can be understood in terms of screening by increasing the core-hole charge in the vicinity of Y.[30] Further, a slight shift of the edge onset to lower energy is also discernible, consistent with a modest narrowing of the conduction band onset and the modified core-hole charge.[30,33,34]

In summary, these signatures reflect the change in bandgap and the local strain acting on the bonding environments around nitrogen within the crystalline areas from which the spectra were acquired. The persistence of the fine structure of the edge to $x = 0.21$ nevertheless implies that a significant fraction of N atoms remain in tetrahedral coordination, inline with the structural evidence of residual wurtzite-type areas near the AlN seed.

12 August 2026 04:35:45

© Author(s) 2026

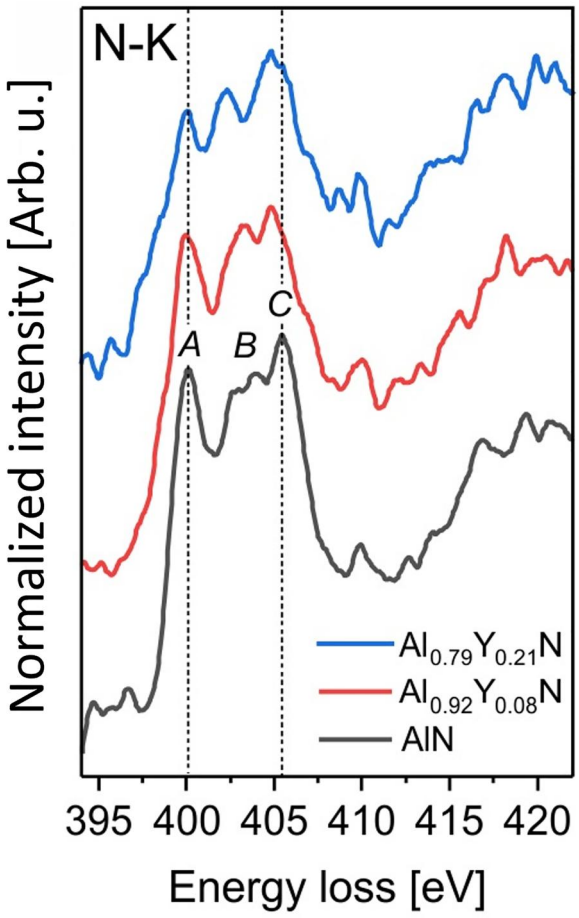

FIG. 8. Electron energy loss spectra of the N-K edge recorded on $Al_{1-x}Y_xN$ layers. The spectra intensity was normalized to the average intensity of the plateau between 418 and 428 eV.

V. EFFECT OF SUBSTITUTION OF STIFF AlN HOST LATTICE WITH SOFT InN

A central hypothesis of this work, introduced in the "Introduction," is that the severe atomic radius mismatch between Al and Y and its interplay with oxygen contamination generate internal strain that ultimately drives the amorphization of $Al_{1-x}Y_xN$ at relatively low Y contents. If the magnitude of this mismatch is a dominant factor, replacing the stiff AlN host with a larger and softer lattice should alleviate the strain and allow a higher fraction of Y to be incorporated while retaining the wurtzite structure. InN is an ideal candidate. Its basal lattice parameter ($a = 351.8$ pm)[35] and c axis parameter ($c = 569.0$ pm)[35] are considerably larger than those of AlN, and its elastic coefficients ($C_{11} = 232$ GPa, $C_{33} = 231$ GPa)[36] are roughly a factor of two lower, indicating a markedly softer matrix.

A series of $In_{1-x}Y_xN$ films (x = 0–0.5) was deposited using magnetron sputtering. XRD measurements were performed on the films. Figure 9 shows the symmetric $2\theta/\theta$ scans around the 0002 reflection of the wurtzite phase. With increasing Y content, the 0002 peak shifts to higher 2θ values, demonstrating a contraction of the out-of-plane lattice spacing c as the larger Y atoms replace In. As the Y content approaches the predicted structural phase transition composition, approximately $x = 0.5$,[15] the diffraction peaks become significantly broader and their intensity decreases, indicating a pronounced degradation of crystalline quality. This behavior reflects the increasing lattice distortion with increasing Y incorporation which disrupts the periodic arrangement and results in partially disordered regions. Nevertheless, the persistence of a weak but still distinguishable diffraction peak close to the phase transition composition indicates that remnants of the wurtzite structure are still present. This suggests that the film does not become fully amorphous at this stage, but rather consists of a mixture of highly disordered crystalline phases along with some amorphous regions. Such behavior is a characteristic of a gradual structural breakdown near the phase boundary and has been reported in related ternary nitride systems such as $In_{1-x}Sc_xN$ and $Al_{1-x}Sc_xN$.[25,37]

To obtain the in-plane lattice parameter a, asymmetric scans were recorded. The extracted lattice parameters are compiled in Fig. 10. The experimental values from this work are in good agreement with the previously reported DFT and experimental data.[15]

The DFT studies reported in previous literature predict that the wurtzite phase of $In_{1-x}Y_xN$ remains thermodynamically stable up to a Y fraction of $x = 0.5$. Experimentally, we have now demonstrated that the wurtzite structure can be preserved in $In_{1-x}Y_xN$ up to the compositional limit predicted by theory. In the $Al_{1-x}Y_xN$ system, the rapid loss of crystallinity is observed already at $x = 0.21$, confirmed through TEM analysis, and at concentrations

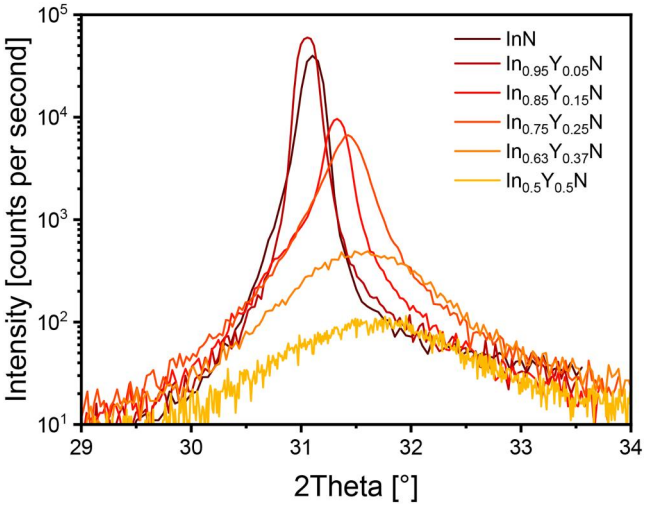

FIG. 9. XRD measurements done on the (0002) crystalline plane of wurtzite $In_{1-x}Y_xN$ with varying Y concentrations.

12 August 2026 04:35:45

© Author(s) 2026

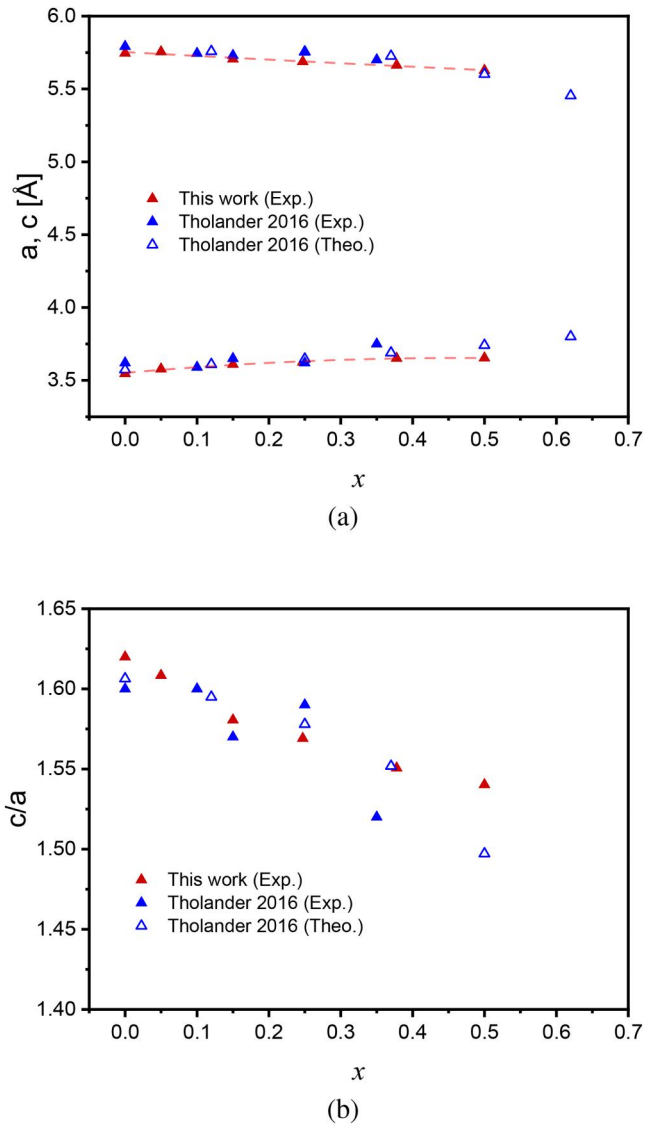

FIG. 10. (a) Extracted lattice parameters *a* and *c* of wurtzite $In_{1-x}Y_xN$ from this work (red) and previously reported DFT and experimental data[15] (blue) and (b) their corresponding ratios.

in the range of $x \sim 0.5$, the amorphization is complete through the whole layer that not even weak diffraction peaks in the XRD data can be seen. This behavior persists despite extensive optimization of growth conditions, including variations in temperature, pressure, and deposition technique. Indeed, previous studies have reported the amorphization[12] or the emergence of cubic phases in $Al_{1-x}Y_xN$ at Y concentrations as low as $x \sim 0.3$, even when using alternative growth approaches such as MOCVD,[10] further underlying the instability of the wurtzite phase in this system. In contrast, for $In_{1-x}Y_xN$, although a significant degradation of crystalline quality is observed with increasing Y content, as reflected by peak broadening and a strong reduction of diffraction intensity (Fig. 9), the persistence of measurable diffraction peaks even near the predicted phase transition composition indicates that crystalline regions are still present. This suggests that, unlike $Al_{1-x}Y_xN$, the structural breakdown in $In_{1-x}Y_xN$ occurs more gradually, allowing remnants of the wurtzite structure to be retained close to the transition point.

The contrasting behavior equivalently point to the internal strain generated by the Al-Y size mismatch as the key destabilizing factor in $Al_{1-x}Y_xN$. When the host lattice is replaced by InN, the lattice mismatch between the host cation and Y is reduced. In addition, the lower elastic modulus of InN allows the alloy to relax the residual strain more efficiently. Consequently, the alloy can accommodate a much larger Y fraction without loosing its long-range order. These results, along with the observations on the positive effect of strain engineering on the stabilization of $Al_{1-x}Y_xN$ at higher Y concentrations provided in our previous work,[2] in which low-Y layers were used as a buffer for the growth of high-Y films, provide a decisive experimental validation of the strain-driven amorphization model proposed for $Al_{1-x}Y_xN$. By selecting a host lattice with larger equilibrium lattice constant and reduced stiffness, the adverse effect of atomic radius mismatch can be mitigated, thereby extending the solubility limit of Y in the wurtzite framework. The successful growth of crystalline $In_{1-x}Y_xN$ up to $x = 0.5$ demonstrates that strain-engineering alone may be insufficient for highly mismatched systems and that the intrinsic compliance of the host lattice is equally important.

VI. CONCLUSION

In this study, we have comprehensively examined the structural evolution of $Al_{1-x}Y_xN$ thin films grown under controlled sputtering conditions in a UHV chamber. By employing a nitrogen-rich reactive gas (NH_3) and carefully optimizing the deposition parameters, extrinsic contamination was minimized and the growth environment was made as favorable as possible. Nevertheless, the fundamental trend observed for the $Al_{1-x}Y_xN$ series remained unchanged with respect to earlier work performed under less demanding conditions. Depth-resolved ToF-SIMS data revealed that both Al and Y are distributed homogeneously throughout each layer; no Y-rich segregation or compositional gradient could be detected, indicating that the films are chemically uniform. TEM measurements showed that the wurtzite structure persists up to roughly $x = 0.1$, but a clear onset of partial amorphization is already evident at $x = 0.21$. At a Y content of $x = 0.5$, the layer is fully amorphous, which is corroborated by the absence of any Bragg reflections in the XRD patterns and by diffuse electron diffraction rings. In contrast, the series of $In_{1-x}Y_xN$ films under similar conditions retained the wurtzite structure up to the highest investigated substitution level of $x = 0.5$. The experimental solubility limit, thus, coincides with the composition at which the DFT formation-energy curves anticipate the hexagonal to cubic phase transition, confirming that the wurtzite phase can be stabilized far beyond the limit observed for $Al_{1-x}Y_xN$. These complementary observations collectively support a conclusion. The internal strain generated by the large atomic radius mismatch between Al and Y

12 August 2026 04:35:45

© Author(s) 2026

is likely the primary factor that destabilizes the wurtzite lattice of $Al_{1-x}Y_xN$, causing premature amorphization even when external growth conditions are optimized. Replacing the stiff AlN host with the softer InN lattice extends the solubility of Y. Consequently, both strain- and host-lattice-engineering emerge as effective strategies in nitride alloys. Future work will focus on probing the piezoelectric and optical properties of the high-Y $In_{1-x}Y_xN$ alloys, exploring additional compliant hosts (such as GaN) to further broaden the Y solubility window, and employing advanced strain-relief techniques to stabilize $Al_{1-x}Y_xN$ at high Y contents.

ACKNOWLEDGMENTS

The authors acknowledge the Gips-Schüle Foundation and the German Science Foundation (DFG) who supported this work through Project No. 562499410, Project No. 286471992 (SFB 1261—Biomagnetic Sensing), Project No. 563148605 (SPP2477—Nitrides4Future), and Project No. 462722619 (SPP2312—GaNius).

AUTHOR DECLARATIONS

Conflict of Interest

The authors have no conflicts to disclose.

Author Contributions

N. Afshar: Conceptualization (lead); Data curation (lead); Formal analysis (lead); Investigation (equal); Methodology (equal); Resources (equal); Validation (lead); Visualization (equal); Writing – original draft (lead); Writing – review & editing (equal). **N. Wolff:** Data curation (equal); Formal analysis (equal); Investigation (equal); Methodology (equal); Resources (equal); Validation (equal); Visualization (equal); Writing – review & editing (equal). **F. Hörich:** Data curation (equal); Formal analysis (equal); Investigation (equal); Methodology (equal); Resources (equal); Validation (equal); Writing – review & editing (equal). **P. Straňák:** Data curation (equal); Formal analysis (equal); Investigation (equal); Methodology (equal); Resources (equal); Validation (equal); Visualization (supporting); Writing – review & editing (equal). **L. Kirste:** Funding acquisition (supporting); Project administration (supporting); Resources (equal); Supervision (supporting); Writing – review & editing (equal). **L. Kienle:** Funding acquisition (supporting); Project administration (supporting); Resources (equal); Supervision (supporting); Writing – review & editing (equal). **A. Dadgar:** Conceptualization (supporting); Formal analysis (supporting); Funding acquisition (equal); Methodology (supporting); Project administration (equal); Resources (equal); Supervision (supporting); Validation (supporting); Writing – review & editing (equal). **O. Ambacher:** Conceptualization (supporting); Data curation (supporting); Formal analysis (supporting); Funding acquisition (lead); Project administration (lead); Resources (equal); Supervision (lead); Validation (equal); Visualization (supporting); Writing – review & editing (equal).

DATA AVAILABILITY

The data that support the findings of this study are available from the corresponding author upon reasonable request.

REFERENCES

[1]S. Pandit, M. Schneider, S. Schwarz, and U. Schmid, "Enhancement of piezoelectric response in yttrium aluminum nitride ($Y_xAl_{1-x}N$) thin films," Adv. Eng. Mater. **25**, 2300940 (2023).
[2]N. Afshar, M. Yassine, A. Yassine, N. Maier, and O. Ambacher, "Electrical and structural characterization of YAlN at high alloy concentrations," J. Appl. Phys. **136**, 185103 (2024).
[3]D. Wang, S. Mondal, J. Liu, M. Hu, P. Wang, S. Yang, D. Wang, Y. Xiao, Y. Wu, T. Ma *et al.*, "Ferroelectric YAlN grown by molecular beam epitaxy," Appl. Phys. Lett. **123**, 033504 (2023).
[4]I. Streicher, P. Straňák, L. Kirste, M. Prescher, S. Müller, and S. Leone, "Two-dimensional electron gases in AlYN/GaN heterostructures grown by metal-organic chemical vapor deposition," APL Mater. **12**, 051109 (2024).
[5]M. Akiyama, T. Kamohara, K. Kano, A. Teshigahara, Y. Takeuchi, and N. Kawahara, "Enhancement of piezoelectric response in scandium aluminum nitride alloy thin films prepared by dual reactive cosputtering," Adv. Mater. **21**, 593–596 (2009).
[6]S. Fichtner, N. Wolff, F. Lofink, L. Kienle, and B. Wagner, "AlScN: A III-V semiconductor based ferroelectric," J. Appl. Phys. **125**, 114103 (2019).
[7]A. Žukauskaitė, C. Tholander, J. Palisaitis, P. O. Å. Persson, V. Darakchieva, N. B. Sedrine, F. Tasnádi, B. Alling, J. Birch, and L. Hultman, "$Y_xAl_{1-x}N$ thin films," J. Phys. D: Appl. Phys. **45**, 422001 (2012).
[8]I. Streicher, N. Wolff, T. Duarte, O. Rehm, P. Straňák, L. Kirste, M. Prescher, X. Guo, V. Nicolosi, L. Baumgarten, M. Müller, L. Kienle, and S. Leone, "Advancing the growth of GaN on AlScN and AlYN by metal-organic chemical vapor deposition," Adv. Phys. Res. **4**, e2500035 (2025).
[9]K. Nomoto, I. Streicher, T.-S. Nguyen, C. Savant, M. Ramesh, S. Ma, J. Encomendero, L. Kirste, P. Straňák, R. Quay, S. Leone, H. G. Xing, and D. Jena, "MOCVD AlYN/GaN HEMTs with 66.5 mV decade sub-threshold swing and 109 on/off ratio," Appl. Phys. Lett. **126**, 223509 (2025).
[10]S. Leone, I. Streicher, M. Prescher, P. Straňák, and L. Kirste, "Metal-organic chemical vapor deposition of aluminum yttrium nitride," Phys. Status Solidi (RRL)–Rapid Res. Lett. **17**, 2300091 (2023).
[11]D. Solonenko, J. Strube, J. Fammels, E. Fisslthaler, V. Röbisch, K. Howell, T. Sinani, J. Pilz, V. Pashchenko, S. Risquez *et al.*, "AlYN thin films with high Y content: Microstructure and performance," Phys. Status Solidi (RRL)–Rapid Res. Lett. **17**, 2300193 (2023).
[12]X. Jiang, Y. Wu, J. Qi, Y. Liu, Y. Wang, B. Zhou, S. Yu, and X. Zhou, "Preparation and deep-UV solar-blind photovoltaic performance of AlYN-based MSM detector," IEEE Sens. J. **24**, 25581–25589 (2024).
[13]National Center for Biotechnology Information, see https://pubchem.ncbi.nlm.nih.gov/periodic-table/atomic-radius for "Atomic radius in the periodic table of elements" (2025) (6 Aug 2025).
[14]O. Ambacher, S. Mihalic, M. Yassine, A. Yassine, N. Afshar, and B. Christian, "Structural, elastic, and thermodynamic properties of cubic and hexagonal $Sc_xAl_{1-x}N$ crystals," J. Appl. Phys. **134**, 160702 (2023).
[15]C. Tholander, J. Birch, F. Tasnádi, L. Hultman, J. Palisaitis, P. O. Å. Persson, J. Jensen, P. Sandström, B. Alling, and A. Žukauskaitė, "Ab initio calculations and experimental study of piezoelectric $Y_xIn_{1-x}N$ thin films deposited using reactive magnetron sputter epitaxy," Acta Mater. **105**, 199–206 (2016).
[16]C. Höglund, J. Birch, B. Alling, J. Bareño, Z. Czigány, P. O. Å. Persson, G. Wingqvist, A. Zukauskaite, and L. Hultman, "Wurtzite structure $Sc_{1-x}Al_xN$ solid solution films grown by reactive magnetron sputter epitaxy: Structural characterization and first-principles calculations," J. Appl. Phys. **107**, 123515 (2010).

12 August 2026 04:35:45

© Author(s) 2026

[17]C. Tholander, I. A. Abrikosov, L. Hultman, and F. Tasnadi, "Volume matching condition to establish the enhanced piezoelectricity in ternary $(Sc,Y)_{0.5}(Al,Ga,In)_{0.5}N$ alloys," Phys. Rev. B—Condens. Matter Mater. Phys. **87**, 094107 (2013).
[18]S. Grigoriev, A. Vereschaka, F. Milovich, N. Sitnikov, J. Bublikov, A. Seleznev, and C. Sotova, "Crack formation and oxidation wear in (Cr,Y,Al)N and (Mo,Y,Al)N nanolayer coatings with high content of yttrium," Wear **528–529**, 204989 (2023).
[19]A. C. Hurley, "The binding energy of the nitrogen molecule," Proc. Phys. Soc. Sec. A **69**, 767 (1956).
[20]X. Yang, B. Li, J. Zhou, X. Li, S. Zheng, Y. Liu, Y. Hao, and G. Han, "N penetration enhances vacancy filling, Al/Sc-N bonding, and ferroelectric properties in AlScN films," IEEE Electron Device Lett. **46**, 1753–1756 (2025).
[21]Q. Wang, S. Go, C. Liu, M. Li, Y. Zhu, L. Li, T. H. Lee, and D. K. Loke, "Understanding effect of distortions and vacancies in wurtzite AlScN ferroelectric memory materials: Vacancy-induced multiple defect state types and relaxation dependence in transition energy levels," AIP Adv. **12**, 125303 (2022).
[22]O. Rehm, L. Baumgarten, R. Guido, P. M. Düring, A. Gloskovskii, C. Schlueter, T. Mikolajick, U. Schroeder, and M. Müller, "Long-term stability and oxidation of ferroelectric AlScN devices: An operando hard x-ray photoelectron spectroscopy study," Phys. Status Solidi (RRL)–Rapid Res. Lett. **19**, 2400307 (2025).
[23]K. M. Calamba, J. Salamania, M. P. J. Jõesaar, L. J. S. Johnson, R. Boyd, J. F. Pierson, M. A. Sortica, D. Primetzhofer, and M. Odén, "Effect of nitrogen vacancies on the growth, dislocation structure, and decomposition of single crystal epitaxial $(Ti_{1-x}Al_x)N_y$ thin films," Acta Mater. **203**, 116509 (2021).
[24]F. Hörich, R. Borgmann, J. Bläsing, G. Schmidt, P. Veit, F. Bertram, J. Christen, A. Strittmatter, and A. Dadgar, "Demonstration of lateral epitaxial growth of AlN on Si(1 1 1) at low temperatures by pulsed reactive sputter epitaxy," J. Cryst. Growth **571**, 126250 (2021).
[25]N. Afshar, M. Yassine, W. Liebscher, F. Hörich, A. Dadgar, and O. Ambacher, "Experimental demonstration of wurtzite to rock salt transition and bandgap evolution in $In_{1-x}Sc_xN$ grown by sputtering," J. Appl. Phys. **139**, 015704 (2026).
[26]N. Afshar, M. Yassine, and O. Ambacher, "A comprehensive review of yttrium aluminum nitride: Crystal structure, growth techniques, properties, and applications," Front. Mater. **12**, 1526968 (2025).
[27]V. Serin, C. Colliex, R. Brydson, S. Matar, and F. Boucher, "EELS investigation of the electron conduction-band states in wurtzite AlN and oxygen-doped AlN(O)," Phys. Rev. B **58**, 5106–5115 (1998).
[28]C. W. Pao, P. D. Babu, H. M. Tsai, J. W. Chiou, S. C. Ray, S. C. Yang, F. Z. Chien, W. F. Pong, M.-H. Tsai, C. W. Hsu, L. C. Chen, C. C. Chen, K. H. Chen, H.-J. Lin, J. F. Lee, and J. H. Guo, "Electronic structures of group-III–nitride nanorods studied by x-ray absorption, x-ray emission, and Raman spectroscopy," Appl. Phys. Lett. **88**, 223113 (2006).
[29]D. Holec, R. Rachbauer, D. Kiener, P. D. Cherns, P. M. F. J. Costa, C. McAleese, P. H. Mayrhofer, and C. J. Humphreys, "Towards predictive modeling of near-edge structures in electron energy-loss spectra of AlN-based ternary alloys," Phys. Rev. B **83**, 165122 (2011).
[30]D. Holec, P. Costa, P. Cherns, and C. Humphreys, "Electron energy loss near edge structure (ELNES) spectra of AlN and AlGaN: A theoretical study using the Wien2k and Telnes programs," Micron **39**, 690–697 (2008).
[31]K. Lawniczak-Jablonska, T. Suski, I. Gorczyca, N. E. Christensen, K. E. Attenkofer, R. C. C. Perera, E. M. Gullikson, J. H. Underwood, D. L. Ederer, and Z. Liliental Weber, "Electronic states in valence and conduction bands of group-III nitrides: Experiment and theory," Phys. Rev. B **61**, 16623–16632 (2000).
[32]M. Petrov, D. Holec, L. Lymperakis, J. Neugebauer, and C. J. Humphreys, "Strain-induced effects on the electronic structure and N K-edge ELNES of wurtzite AlN and $Al_xGa_{1-x}N$," J. Phys.: Conf. Ser. **326**, 012016 (2011).
[33]N. B. Sedrine, A. Zukauskaite, J. Birch, L. Hultman, and V. Darakchieva, "Bandgap engineering and optical constants of $Y_xAl_{1-x}N$ alloys," Jpn. J. Appl. Phys. **52**, 08JM02 (2013).
[34]Y. Xie, Y. Cai, Y. Liu, Y. Zhao, S. Guo, C. Sun, and S. Liu, "Electronic structure and optical properties of YAlN: A first-principles study," Phys. Status Solidi (b) **257**, 1900678 (2020).
[35]C. K. Gan and D. J. Srolovitz, "First-principles study of wurtzite InN (0001) and (0001) surfaces," Phys. Rev. B—Condens. Matter Mater. Phys. **74**, 115319 (2006).
[36]M. M. Soumelidou, I. Belabbas, J. Kioseoglou, P. Komninou, J. Chen, and T. Karakostas, "Strain and elastic constants of GaN and InN," Comput. Condens. Matter **10**, 25–30 (2017).
[37]Y. Zhao, J. Sui, D. Zhou, Y. Tong, Q. Kou, and J. Xi, "Phase transition, leakage, dielectric permittivity and polarization switching of $Al_{1-x}Sc_xN$ films in a wide Sc concentration range," Ceram. Int. **51**, 5038–5044 (2025).

12 August 2026 04:35:45

© Author(s) 2026